PCCP

ROYAL SOCIETY OF CHEMISTRY

PAPER

Published on 31 July 2026

Cite this: DOI: 10.1039/d6cp02388f

Rationalizing the fluorescence emission enhancement of imidazo[1,5-*a*]pyridines in the solid state upon hydrogenation

Chiara Vola,[a] G. Attilio Ardizzoia,[a] Anita Cinco,[ab] Gioele Colombo,*[a] Bruno Therrien[c] and Stefano Brenna[a]

Received 24th June 2026,
Accepted 25th July 2026

DOI: 10.1039/d6cp02388f

rsc.li/pccp

The development of organic materials with high quantum efficiency in the solid state remains a significant challenge, particularly for deep-blue emitters. In this work, we investigate the solid-state photophysical properties of a series of hydrogenated imidazo[1,5-*a*]pyridine derivatives, which exhibit exceptional deep-blue fluorescence with absolute photoluminescence quantum yields (PLQYs) up to 0.96. This intense emission is highly counterintuitive when compared to their fully conjugated counterparts, which are nearly non-emissive in the crystalline phase. Through a detailed comparative analysis and Hirshfeld surface investigations, we demonstrate that the high efficiency of the hydrogenated species is rooted in their specific crystalline arrangement. While the aromatic precursors are characterized by strong intermolecular hydrogen bonds and H–π interactions that activate non-radiative decay pathways, the hydrogenated derivatives adopt a packing motif dominated by non-directional H–H interactions and intramolecular hydrogen bonds. This structural alteration effectively suppresses detrimental quenching mechanisms, allowing the radiative transition to dominate. We define this phenomenon as packing-induced fluorescence enhancement (PIFE). These results provide critical insights into the rational design of high-efficiency solid-state emitters for optoelectronic applications, such as luminescent down shifting (LDS) layers for photovoltaics and active layers in blue OLEDs.

Introduction

Low-cost organic dyes have recently attracted considerable attention due to their versatility and wide range of potential applications in optoelectronics. In particular, one of their most promising uses is as Luminescent Down Shifting (LDS) materials.[1–3] When applied as a luminescent coating on the surface of photovoltaic devices, LDS layers can overcome the intrinsic limitation of solar cells in harvesting high-energy photons. Conventional solar cells, indeed, show a reduced spectral response in the ultraviolet and blue regions of the spectrum, which leads to significant energy losses.[4–6] LDS materials address this issue by absorbing high-energy photons, inefficiently captured by the active layer,[7,8] and re-emitting them at longer wavelengths, where the cell exhibits higher absorption efficiency. For this strategy to be effective, LDS candidates should combine a broad absorption band in the UV-visible range (300–400 nm), a high molar extinction coefficient, a large Stokes shift to minimize reabsorption, and, ideally, low cost and ease of processing.[9,10] Organic dyes often meet these requirements,[11–13] making them highly appealing for large-scale photovoltaic applications.

At the same time, organic luminescent materials have found wide application in the opposite process: the conversion of electrical energy into light, as exploited in organic light emitting diodes (OLEDs).[14,15] Over the past two decades, OLED technology has revolutionized the field of optoelectronics, becoming popular in displays, solid-state lighting, and sensor devices.[16] Compared to traditional lighting technologies, OLEDs provide several advantages, including high luminous efficiency,[17,18] low power consumption,[19] mechanical flexibility[20,21] and the possibility to fabricate ultrathin and lightweight devices by solution processing[22,23] or vacuum deposition.[24,25] Nevertheless, the overall device efficiency and stability are strongly dependent on the performance of the luminescent material employed in the emissive layer, which plays a central role in dictating both color purity and energy conversion efficiency.[26,27] For this reason, the design and synthesis of new efficient and stable emitters remain an area of intense research interest.[28–31]

[a] *Department of Science and High Technology, University of Insubria and CIRCC, Via Valleggio, 9, 22100 Como, Italy. E-mail: gioele.colombo@uninsubria.it; Fax: +39-(0)31-2386119; Tel: +39-(0)31-2386476*

[b] *University School for Advanced Studies IUSS, Palazzo del Broletto, Piazza Vittoria 15, 27100 Pavia, Italy*

[c] *Institute of Chemistry, Université de Neuchâtel, Avenue de Bellevaux 51, CH-2000 Neuchâtel, Switzerland*

Despite remarkable progress, significant challenges persist in OLED development.[32,33] The fabrication of efficient and stable blue-emitting devices is particularly demanding compared to their green and red counterparts.[34,35] Blue-emitting materials suffer from lower efficiency and reduced operational lifetimes, which directly limit device performance and commercialization potential. Achieving efficient blue emission requires careful molecular design to balance several critical parameters,[36] including appropriate frontier orbital energies for balanced charge injection and recombination, emission coordinates close to the CIE standard blue, high photoluminescence quantum yield, and robust long-term stability. These requirements render the search for suitable blue emitters especially challenging.[37–39]

In this context, imidazo[1,5-*a*]pyridines represent a class of heteroaromatic compounds that has drawn considerable attention in both academic and industrial settings. Initially recognized for their broad pharmacological activities[40,41] and synthetic accessibility,[42,43] these systems have more recently attracted interest for their intriguing photophysical behavior,[44–46] such as large Stokes shifts, good to high fluorescence quantum yields and great photostability. Such dual interest, spanning from medicinal chemistry to materials science, highlights the versatility of this scaffold.[47]

Building on these foundations, our group has been exploring the photophysical properties of imidazo[1,5-*a*]pyridine derivatives for years.[48–53] Remarkably, we observed that hydrogenation of the pyridinic ring leads to a new class of compounds with outstanding optical characteristics.[54,55] In solution, these hydrogenated derivatives display intense fluorescence with high quantum yields and, notably, deep blue emissions that are rare and highly sought after in optoelectronic applications. In addition to their excellent photophysical profile, the efficient and cost-effective synthetic procedures employed to obtain these compounds further enhance their practical potential. In this study, we present a detailed investigation of the solid-state photophysical behavior of hydrogenated imidazo[1,5-*a*]pyridines, looking for structure–property relationships that are crucial for the understanding of such peculiar fluorescence enhancement.

Results and discussion

Compounds **1–5** were synthesized following a previously reported procedure (Scheme 1).[54] The synthesis began with the condensation of 2-acetylpyridine and 5-substituted salicylaldehydes, using ammonium acetate as the source of sp^2 nitrogen, to afford the corresponding precursors. These intermediates were then subjected to catalytic hydrogenation with molecular hydrogen (10 atm) in a steel autoclave, employing Pd/C (10% m/m loading) as catalyst. The white solids were analyzed by infrared spectroscopy, elemental analysis, ^{1}H and $^{13}C\{^1H\}$ NMR spectroscopy, confirming their purity and consistency with the literature data.

All the investigated hydrogenated compounds exhibited bright blue fluorescence emission, both in solution[54] and in the solid state (Fig. S1), with the latter generally showing higher intensity. Consequently, their photophysical properties were further evaluated in the solid state (see Fig. 1 for absorption and emission spectra of compound **2a** as a representative example and Fig. S2 for the whole series).

The absorption spectra of the series exhibit comparable features, with two main absorption bands. The first, more intense band appears between 360 and 400 nm, while the second is observed at 325 nm. Notably, the position of the most intense band varies depending on the substituent, whereas the second band remains essentially unchanged. Compound **2e** deviates from this general behavior, showing an absorption maximum at 297 nm accompanied by a weaker shoulder around 350 nm. This behavior can be attributed to the presence of a strongly electron-attracting substituent (CF_3), which induces a hypsochromic shift of the absorption maximum compared to alkyl- or halogen-substituted analogues.[56–58] This leads to significant Stokes shifts, ranging from 3885 to 4515 cm^{-1} for compounds **2a–d**, and exceeding 9000 cm^{-1} for compound **2e**.

In light of these, this lower-energy shoulder could be attributed to an electronic transition with partial intramolecular charge transfer (ICT) character, which is typical of the donor–acceptor molecular architecture inherent to the series, where an electron-donating phenolic moiety is linked to an electron-accepting imidazo[1,5-*a*]pyridine core. It is important to note that this assignment is a qualitative structural inference; standard isolated-molecule theoretical treatments (*e.g.*, TD-DFT) would fail to capture the profound modulation of the frontier orbitals by crystal lattice interactions.

The emission spectra, on the other hand, display maxima between 400 and 500 nm, depending on the substituent at the phenolic ring. A general trend is observed whereby more electron-withdrawing substituents lead to shorter emission

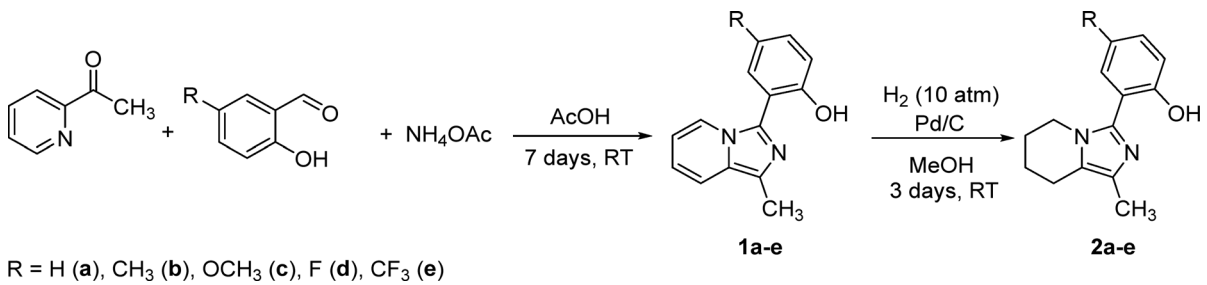

Scheme 1 Synthetic procedure to obtain compounds **1a–e** and **2a–e**.

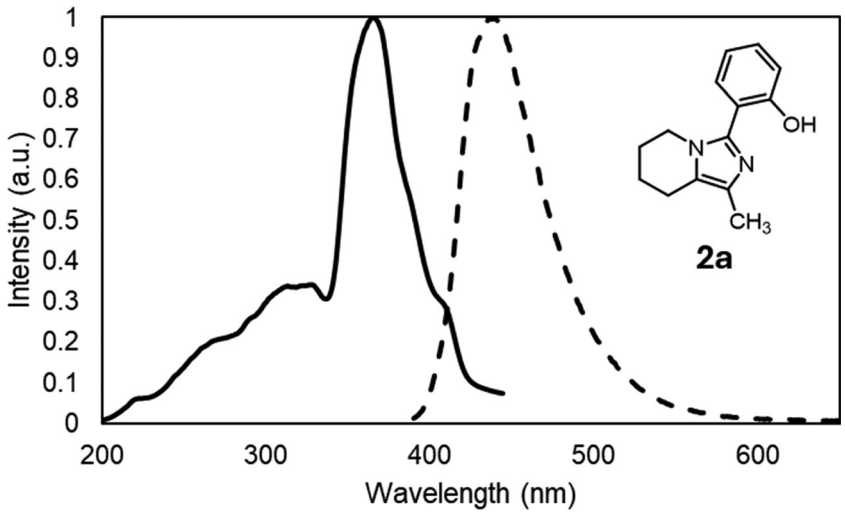

Fig. 1 Absorption (solid line) and emission (dashed line) spectra of compound **2a** recorded in solid state.

wavelengths (Fig. S3). Compound **2e** again represents an exception, exhibiting a partially resolved vibrational structure in its emission band. Fluorescence decays were best fitted with a bi-exponential model, with short-lived components ranging from 1.6 to 5.7 ns and longer-lived components from 3.8 to 10.1 ns (Fig. S4). Fluorescence quantum yields were generally high, spanning from 0.24 to 0.96.

The observed biexponential fluorescence decay suggests the presence of at least two emissive environments. A plausible interpretation is that the shorter lifetime component originates from molecules located at crystal surfaces or defect-rich regions, where non-radiative relaxation is enhanced, whereas the longer lifetime component is associated with molecules embedded in the more ordered bulk crystal lattice.[59–61]

A complete summary of the photophysical data is provided in Table 1.

Notably, the fluorescence quantum yields of these compounds in the solid state are markedly enhanced compared to their non-hydrogenated counterparts, which are very weakly emissive ($\Phi_{FL} < 0.05$). This observation may appear counter-intuitive, as hydrogenation reduces the extent of conjugation and would therefore be expected to diminish, rather than improve, the emission efficiency of these species.[62] Furthermore, the presence of more aliphatic C–H bonds, should reduce the fluorescence quantum yield due to vibrational quenching.[63,64] Therefore, a deeper structural analysis has been carried out in order to rationalize this behavior.

Crystals of compounds **2a** and **2c** were obtained by slow evaporation of a saturated hexane solution and were subsequently used for X-ray crystal structure determination. In parallel, the corresponding non-hydrogenated derivative **1a** was also crystallized from slow evaporation from a saturated dichloromethane solution. All compounds exhibited bond lengths and angles comparable to those reported for structurally related molecules.[47] Compounds **2a** and **2c** clearly adopt a half-chair conformation for the piperidinyl rings, whereas the pyridinic ring in **1a** is planar (Fig. 2). Interestingly, differences are observed when comparing the angles between the phenol and imidazolic moieties: the hydrogenated compounds **2a** and **2c** exhibit angles of 21.8° and 11.6°, respectively, while the corresponding angle in the non-hydrogenated **1a** is 59.9° (Fig. S5).

The smaller angles between the two moieties in the hydrogenated species could, in principle, promote intermolecular

Table 1 Photophysical data of compounds **2a–e** recorded in solid state. k_r and k_{nr} have been calculated using the average lifetime. Data for compounds **1a–e** are not reported as they are almost non-emissive

Compd	λ_{Abs} (nm)	λ_{Em} (nm)	Stokes shift (nm)	Stokes shift (cm^{-1})	Stokes shift (eV)	τ (ns)	τ (ns) (average)	Φ_{FL}[a]	k_r ($\times 10^8$)	k_{nr} ($\times 10^8$)
2a	366	437	71	4439.11	0.55	1.6 (24.5%) 3.6 (75.5%)	3.3	0.79	2.3	0.73
2b	374	450	76	4515.75	0.56	3.9 (25.3%) 6.3 (74.7%)	5.7	0.37	0.7	1.1
2c	396	468	72	3885.00	0.48	5.7 (84.0%) 10.1 (16.0%)	6.4	0.95	1.5	0.06
2d	379	452	73	4261.33	0.53	3.1 (28.3%) 5.8 (71.7%)	5.0	0.95	1.9	0.10
2e	297	406	109	9039.49	1.12	4.2 (40.1%) 6.6 (59.9%)	5.6	0.24	0.4	1.4

[a] Φ_{FL} values are reported with an experimental uncertainty of ±0.05.

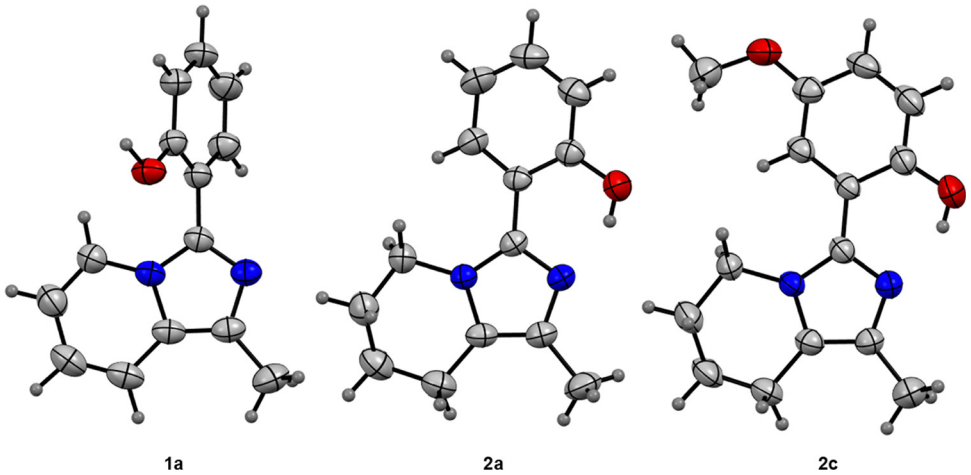

Fig. 2 Crystal structure of compounds **1a**, **2a** and **2c** displayed as thermal ellipsoid at a 50% probability level (pale grey, hydrogen; grey, carbon; blue, nitrogen; red, oxygen).

interactions such as π–π stacking. In compound **2c**, the distance between two stacked imidazolic rings was calculated to be 3.75 Å (centroid–centroid), whereas in compound **2a**, which is slightly less planar, the corresponding distance is 3.87 Å (Fig. S6). In both cases, the imidazolic rings do not stack in a perfectly parallel fashion but rather in a staggered arrangement, leading to virtually infinite stacks along the *a*-axis (Fig. S7). Such interactions would be expected to enhance non-radiative decay pathways, thereby reducing the fluorescence performance (*i.e.*, quantum yields) of these systems in the solid state when compared to non-hydrogenated derivative **1a**. Here, π–π stacking is only possible between two molecules (centroid–centroid distance 3.77 Å, Fig. S6), reasonably due to the increased perpendicularity between the planes described above (59.9° between phenol and imidazopyridinic portion, to be compared with 21.8° and 11.6° in the hydrogenated species) preventing the formation of the aforementioned infinite stacks. To better understand how intermolecular interactions affect emission intensity in these species, a deeper structural investigation has been carried out using Hirshfeld's potential surface analysis.[65]

The Hirshfeld surface analysis provides valuable insight into the intermolecular interactions governing the packing of the two investigated derivatives, **2a** and **2c**. In the case of **2a** (Fig. 3),

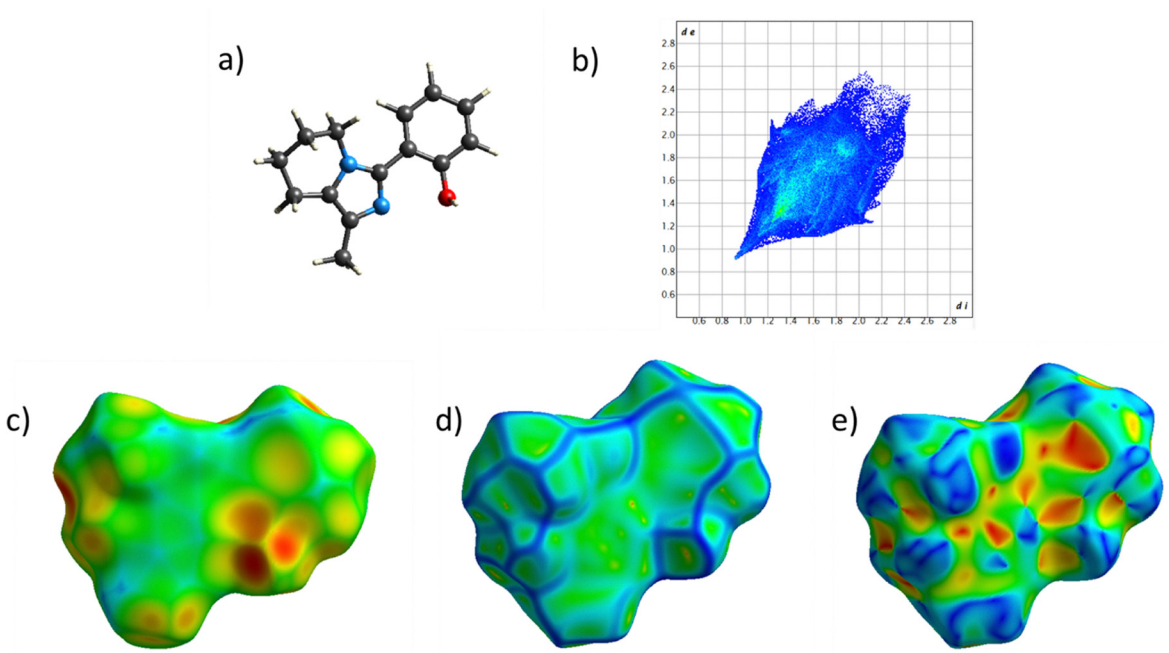

Fig. 3 Hirshfeld surface analysis for compound **2a**: (a) molecular orientation; (b) fingerprint plot; (c) Hirshfeld surface plotted with the d_e color map; (d) Hirshfeld surface plotted with the curvedness color map; (e) Hirshfeld surface plotted with the shape index color map.

the fingerprint plot clearly shows that the crystal packing is dominated by H–H interactions (Fig. 3b), which account for as much as 64.4% of the total contacts. These interactions are evidenced by the numerous intense red spots on the d_e surface (Fig. 3c), particularly in the regions close to the oxygen atom. At first glance, such features might suggest the presence of hydrogen bonds; however, a more careful inspection of the fingerprint plot confirms that they are better attributed to H–H contacts. Only a limited number of O–H interactions (6.1%) can be identified, and even these appear to be weak and often overshadowed by the neighboring C–H and H–H contacts. The curvedness surface of **2a** (Fig. 3d) highlights a relatively flat red area around the carbon atom of the phenolic ring bonded to the imidazole moiety. This feature can reasonably be explained by the presence of a hydrogen atom from a neighboring molecule pointing directly toward this carbon atom, reinforcing the idea of close H–C or H–H interactions rather than directional hydrogen bonding. The shape index (Fig. 3e), in turn, does not display the typical triangular motifs that would indicate π–π stacking. This absence is corroborated by the fingerprint plot (Fig. 4), which reveals only a negligible fraction of C–C (π–π) interactions (2.0%). A notable feature is the large red patch at the center of the phenyl ring, which can be assigned to the interaction with the hydrogen atom in the para position to the hydroxyl group of a neighboring molecule. Overall, the lower face of the molecule does not display particularly remarkable features, although an orange patch on the oxygen atom may still suggest the presence of a weak hydrogen bond. Collectively, these observations indicate that **2a** has a packing arrangement largely determined by non-directional H–H contacts, with only marginal contributions from more specific interactions.

The situation changes when considering derivative **2c**. Here, the Hirshfeld surface once again shows dominant H–H interactions (58.0%), but their relative importance is reduced compared to **2a**. More significant is the contribution of O–H contacts, which represent 14.6% of the total interactions. Remarkably, about 11% of these originate directly from the

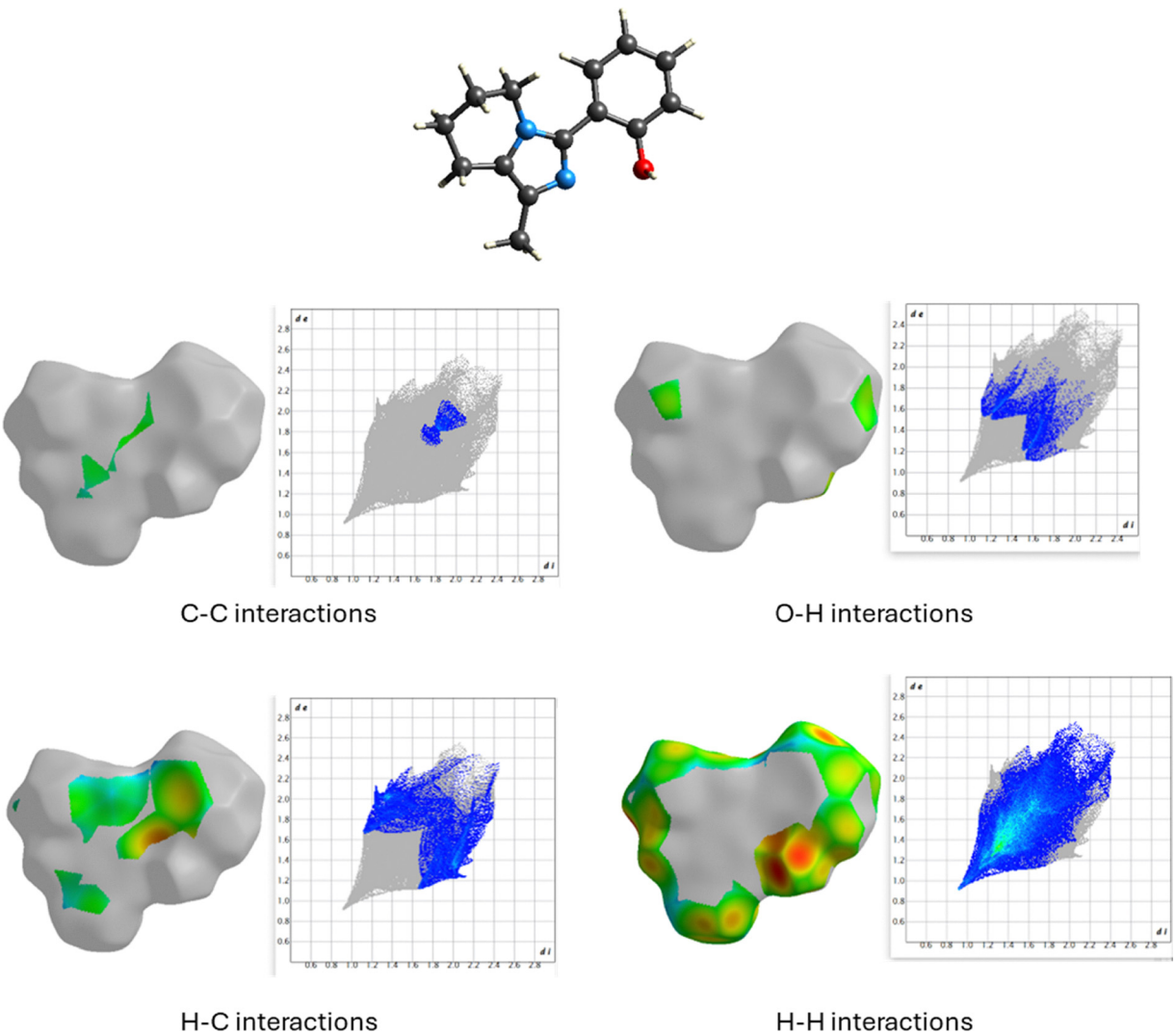

Fig. 4 Hirshfeld surface analysis of **2a** displaying the regions where the different interactions take place.

phenolic hydroxyl group, underlining its important role in directing molecular packing. This feature distinguishes **2c** from **2a**, where the hydroxyl group was far less involved in the crystal lattice. In addition, H–C (H–π) interactions are slightly more pronounced (19.5%) in **2c**, and they are visible in the fingerprint plot (Fig. S8b) as distinct "wings" corresponding to two different types of H–π contacts. The curvedness surface of **2c** appears more fragmented (Fig. S8d), with several red patches suggesting closer intermolecular proximities than those observed in **2a**. This pattern is consistent with a more efficient packing arrangement, an interpretation further supported by the fingerprint analysis. Despite this improved packing, the shape index (Fig. S8e) again does not reveal any characteristic features of π–π stacking, confirming that aromatic–aromatic interactions are negligible (1.6%) (Fig. S9). However, red regions over the phenolic ring highlight the presence of H–π interactions, which likely play a compensatory role in the absence of significant π–π overlap. The lower molecular surface does not reveal major differences with respect to **2a**, although the overall distribution of contacts suggests a slightly more compact organization.

Moving to the non-hydrogenated derivative **1a**, the nature of the intermolecular interactions changes significantly. In this case, intermolecular hydrogen bonds play a prominent role in the crystal packing, as evidenced by the characteristic set of spikes in the bottom left-hand corner of the fingerprint plot (Fig. 5b). Specifically, the hydroxyl group is oriented toward the imidazolic nitrogen atom of a neighboring molecule, a feature clearly highlighted by the intense red spot on the d_e-mapped Hirshfeld surface (Fig. 5c) localized on the nitrogen atom. This interaction represents the main difference with respect to the crystal packing observed for the hydrogenated analogue, accounting for 10.5% of the total interactions (Table 2).

As observed for compounds **2a** and **2c**, only limited direct π–π overlap between aromatic rings is present in the crystal structure, with an interplanar distance of approximately 3.80 Å. In contrast, H–π interactions emerge as an important stabilizing contribution (27.9%). In particular, the hydrogen atoms at positions 3 and 4 of the phenolic rings are oriented toward the centroids of the imidazolic and pyridinic rings, respectively, with H–centroid distances of 2.85 and 2.71 Å. These interactions are also evident on the d_e-mapped surface as two yellow regions located over the corresponding aromatic rings.

The curvedness-mapped surface (Fig. 5d) suggests the presence of an additional H–O interaction between the hydroxylic oxygen atom and a pyridinic hydrogen. Similarly, the shape index-mapped surface (Fig. 5e) reveals a slightly more pronounced contribution from π–π stacking interactions, as indicated by the characteristic complementary red and blue patterns. These features are further supported by the fingerprint plot (Fig. 6), where in particular the H–O interaction corresponds to the second, less intense set of spikes in the bottom left-hand corner and is visualized as a yellow region centered on the oxygen atom.

In terms of molecular descriptors (Table 2), both the hydrogenated derivatives display very similar volumes and surface areas, with **2c** being slightly larger due to the presence of the methoxy group. The globularity values are practically identical, although **2a** appears marginally more spherical, possibly due to the absence of the methoxy substituent. The asphericity values are likewise comparable, both derivatives lying between isotropic and oblate, with a tendency toward the latter. Compound

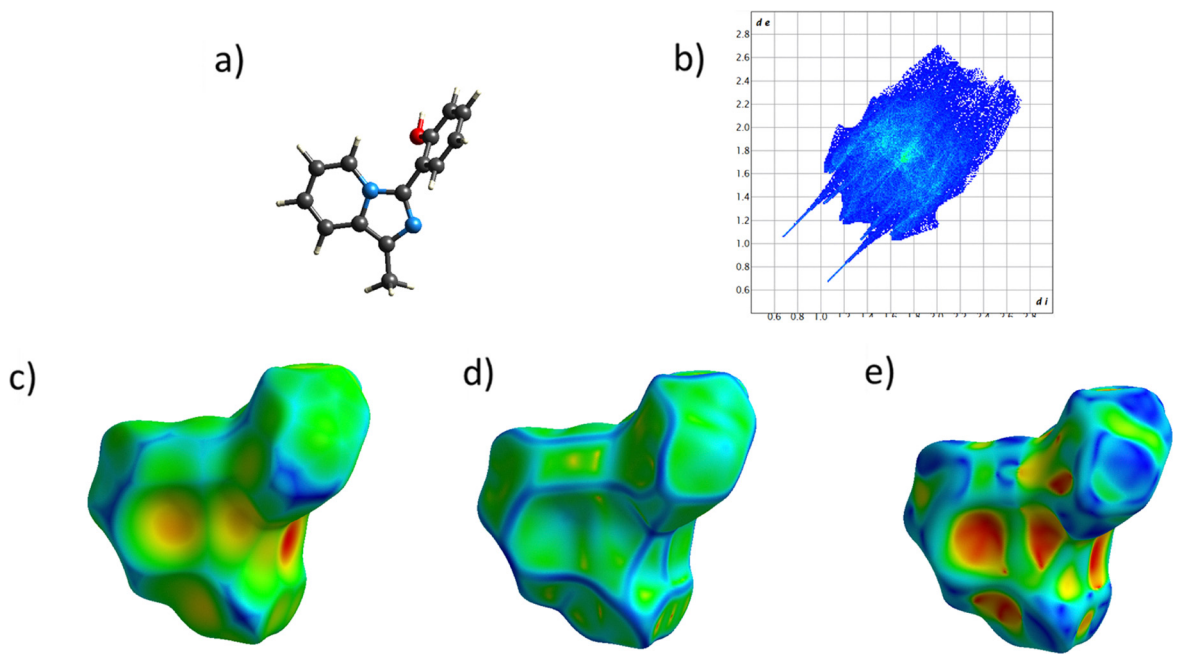

Fig. 5 Hirshfeld surface analysis for **1a**: (a) molecular orientation; (b) fingerprint plot; (c) Hirshfeld surface plotted with the d_e color map; (d) Hirshfeld surface plotted with the curvedness color map; (e) Hirshfeld surface plotted with the shape index color map.

Table 2 Hirshfeld surface analysis parameters retrieved for crystal data of **2a**, **2c** and **1a**

	Compound **2a**	Compound **2c**	Compound **1a**
C–C interactions	2.0%	1.6%	2.9%
H–C interactions	18.9%	19.5%	27.9%
H–H interactions	64.4%	58.0%	51.5%
O–H interactions	6.1%	14.6%	6.2%
N–H interactions	6.5%	3.7%	10.5%
N–N interactions	0.2%	0.2%	—
Other interactions	1.9%	2.4%	1.0%
Volume (Å^3)	281.70	307.92	289.18
Surface (Å^2)	267.57	294.10	278.45
Globularity	0.777	0.750	0.759
Asphericity	0.155	0.159	0.114

1a presents similar values, with an asphericity hinting toward a more isotropic shape, that could lead to a less organized packing, as also corroborated by the diffuse zone in the high d_e and high d_i region of the fingerprint plot (Fig. 5b).

Additionally, to ensure that the bulk powders retain the same crystal packing as the single crystals, emission spectra and PLQY measurements were also recorded on ground single crystals of **2a** and **2c**, yielding identical results.

Considering all the above, the differences in fluorescence intensity observed between the hydrogenated and non-hydrogenated species can be rationalized. Although the hydrogenated derivatives exhibit a higher content of aliphatic C–H groups and an increased molecular planarity compared to their non-hydrogenated counterparts, the latter display similar π–π contacts and a significantly larger number of H–π interactions within the crystal lattice. Both types of intermolecular interactions are known to promote fluorescence quenching in the solid state by facilitating non-radiative deactivation pathways.[66–68]

Structural analysis demonstrated, however, that the dominant contribution to fluorescence quenching can be attributed to the presence of intermolecular hydrogen bonding, which is far more present in the non-hydrogenated species, while almost absent in the hydrogenated ones, in favor of intramolecular hydrogen bond. This additional interaction introduces an efficient non-radiative decay channel,[69–71] outweighing the effects associated with planarity and aliphatic C–H content and ultimately resulting in the reduced fluorescence intensity observed for the non-hydrogenated derivatives.

This highlights the dual role of the phenolic OH group: while its involvement in intermolecular hydrogen bonding acts as a severe fluorescence quencher in the aromatic precursors, its restriction to intramolecular locking in the hydrogenated analogues preserves the radiative path. Consequently, replacing the OH with a non-hydrogen-bond-donating substituent (*e.g.*, OMe) would likely restore fluorescence in the non-hydrogenated series by removing the intermolecular quenching pathway, whereas it should not significantly affect the high emission efficiency of the hydrogenated derivatives.

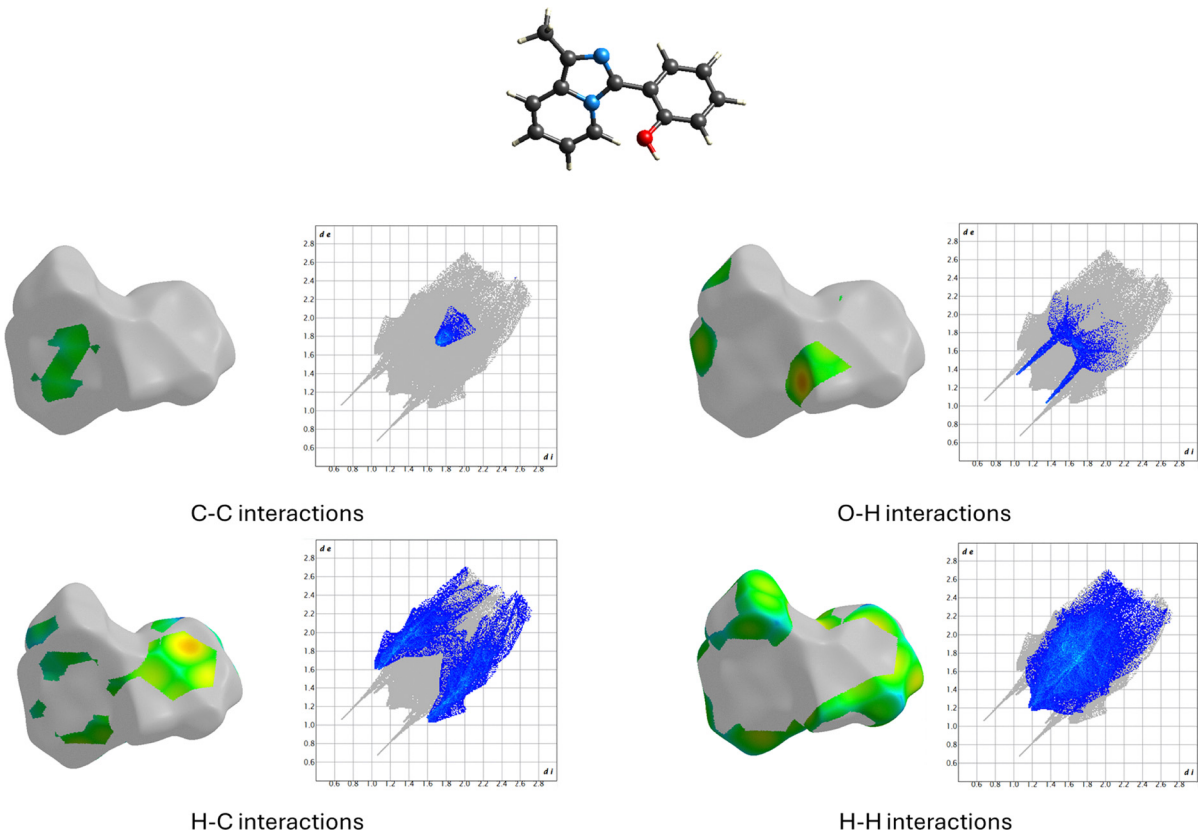

Fig. 6 Hirshfeld surface analysis of **1a** displaying the regions where the different interactions take place.

The influence of the crystal packing on the emission efficiency is quantitatively supported by the radiative (k_r) and non-radiative (k_{nr}) rate constants (Table 1). The most efficient emitters, **2a**, **2c** and **2d** exhibit significantly suppressed non-radiative decay constants. Specifically, **2c** and **2d** achieve the highest PLQY with exceptionally low k_{nr} values, while **2a** also retains a high PLQY and a competitive k_{nr}. Hirshfeld surface analysis reveals that both **2a** and **2c** benefit from a lattice packing dominated by non-directional H–H interactions rather than the strong intermolecular hydrogen bonds or H–π contacts that act as quenching funnels in the non-hydrogenated precursor **1a**. Within this efficient series, the Hirshfeld analysis reveals that **2c** possesses a highly fragmented curvedness surface and a significant structural contribution from the methoxy group, resulting in a highly compact, rigid lattice. This rigidification efficiently suppresses thermal vibrational modes, further minimizing k_{nr} compared to the other derivatives and allowing the radiative process to dominate.

To properly describe the origin of the observed fluorescence enhancement, it is important to clarify that this phenomenon does not correspond to classical aggregation-induced emission (AIE), which involves aggregation of the same molecular species. Here, the increased emission arises instead from differences in crystal packing and intermolecular interactions between closely related solid-state species of the same molecular family.

In this context, we could describe this fluorescence enhancement due to packing-dependent intermolecular interactions within the crystal lattice as a sort of packing-induced fluorescence enhancement (PIFE), a physical phenomenon where fluorescence intensity is governed by the specific supramolecular arrangement of the crystal lattice, rather than by the classic AIE mechanism. While AIE typically involves the restriction of intramolecular motions when moving from solution to the solid state, PIFE operates within the solid state itself by comparing structurally similar molecules with different lattice packings.

Our findings demonstrate that the remarkable fluorescence enhancement observed upon hydrogenation is driven by a transition in the crystal lattice: the non-hydrogenated precursors are dominated by quenching intermolecular hydrogen bonds and H–π interactions, whereas the hydrogenated derivatives are characterized by non-directional H–H interactions that preserve the radiative path. The observed variation in photoluminescence quantum yields (PLQYs) across the series, spanning from 0.24 to 0.95, does not contradict this mechanism: the structural rationale is directly supported by crystallographic and Hirshfeld surface analyses only for compounds **2a** and **2c**, whereas the PLQY variations observed for the remaining derivatives (**2b**, **2d** and **2e**) are attributed to the modulation of emission efficiency by the specific electronic and steric effects of the substituents, as direct structural confirmation is currently limited to the **2a** and **2c** representatives. Indeed, PIFE specifically captures the massive fluorescence enhancement observed when moving from non-emissive precursors **1a-e** to highly emissive hydrogenated species **2a–e**, mediated by the shift in the intermolecular packing motif.

Within this framework, PIFE provides a robust mechanistic basis for understanding the solid-state fluorescence, where the suppression of the primary quenching channels allows for the fine-tuning of emission efficiency through targeted molecular design. Although this model is currently anchored in the comparative behavior of these two specific molecular series, it serves as a foundational platform that warrants further extensive investigation; future work will focus on challenging and expanding this concept to rigorously establish its broader predictive potential across different crystalline architectures.

Experimental section

Materials and methods

Infrared Spectra were acquired on a Shimadzu Prestige-21 spectrometer with a 1 cm^{-1} resolution; elemental analyses were obtained with a PerkinElmer CHN Analyzer 2400 Series II. NMR spectra were recorded with an AVANCE 400 Bruker spectrometer operating at 400 MHz for ^{1}H NMR and 100 MHz for $^{13}C\{^{1}H\}$ NMR. Emission spectra were measured using a fluorescence spectrometer (Edinburgh Instruments FS5) equipped with a 150 W continuous Xenon lamp as a light source and an additional detector for transmittance and were corrected for the wavelength response of the instrument; lifetime measurements were performed on the same FS5 Edinburgh Instruments using an EPLED-320 (Edinburgh Instruments) as the pulsed source. Analysis of the lifetime decay curve was done using Fluoracle® Software package (Ver. 1.9.1) which runs the FS5 instrument. Absolute fluorescence quantum yields were determined on a Photon Technology International (PTI) QuantaMaster QM-40 spectrometer (Xe arc lamp, 70 W) with a PhotoMed GmbH K-Sphere Integrating Sphere (3.2 inch. diameter): integrated intensities have been obtained from the same software running the PTI spectrometer (PTI FeliX32) and used to determine absolute photoluminescence quantum yields in the solid state according to the literature[72] using the equation reported below:

$$\phi_{\theta L} = \frac{E_i(\lambda) - (1 - A) \cdot E_0(\lambda)}{L_e(\lambda) \cdot A}$$

where

$$A = \frac{L_0(\lambda) - L_i(\lambda)}{L_0(\lambda)}$$

$E_i(\lambda)$ = integrated emission under direct excitation of the sample; $E_0(\lambda)$ = integrated emission under secondary excitation of the sample; $L_i(\lambda)$ = integrated excitation under direct excitation of the sample; $L_0(\lambda)$ = integrated excitation under secondary excitation of the sample; $L_e(\lambda)$ = integrated excitation profile of the empty integrating sphere.

To ensure accurate absolute photoluminescence quantum yield measurements, all samples were finely ground using an agate mortar prior to analysis to minimize scattering and reabsorption effects and to ensure a homogeneous particle size. Solid-state UV-vis absorption spectra were recorded on a

Shimadzu UV-2600 spectrophotometer equipped with the relative diffuse reflectance measurement setup. To ensure optimal signal intensity and to prevent detector saturation caused by the high absorbance of the pure compounds, the finely ground samples were diluted in a non-absorbing white matrix of high-purity barium sulfate. Pure $BaSO_4$ powder was used as the 100% reflectance reference standard. The measured diffuse reflectance data were converted into absorption-like spectra using the Kubelka–Munk transformation implemented in the software running the spectrophotometer (UVProbe v. 2.70). All the chemicals were of reagent grade quality and were purchased commercially (AlfaAesar, Acros, TCI Chemicals, Fluorochem) and used as received.

X-ray structure determination

Crystals of **1a**, **2a** and **2c** were mounted on a STOE IPDS II image plate diffractometer (Darmstadt, Germany) equipped with a ϕ circle goniometer, using Mo-Kα graphite monochromated radiation (λ = 0.71073 Å) with ϕ range 0–200°. The structures were solved and refined by direct methods using the OLEX2 platform.[73] The H-atoms were included in calculated positions and treated as riding atoms for **2a** and **2c**, but located and refined for **1a**, while the non-H atoms were refined anisotropically, using weighted full-matrix least-square on F^2. Crystallographic details are summarized in Table S1. Fig. 2 was drawn with Mercury.[74]

CCDC 2535601 (**1a**), 2535602 (**2a**) and 2535603 (**2c**) contain the supplementary crystallographic data for this paper.

The intermolecular interactions within the crystal structure are quantified and visualized using Hirshfeld surfaces computational method calculated using CrystalExplorer.[75]

Conclusions

A comprehensive investigation into the solid-state photophysical properties of a series of hydrogenated imidazo[1,5-*a*]pyridine derivatives has been reported. The findings demonstrate that the partial saturation of the pyridinic ring yields compounds characterized by intense, high-energy deep-blue fluorescence, with absolute quantum yields reaching as high as 0.96. This result is particularly significant given the reduction in conjugation and the introduction of potentially deactivating aliphatic C–H bonds, which would typically suggest a decrease in emissive efficiency. The rationalization of this counterintuitive enhancement was achieved through a detailed structural analysis and the study of Hirshfeld surfaces. We have shown that the nearly complete absence of emission in the non-hydrogenated precursors is not a result of classic aggregation-caused quenching, but is instead driven by the specific crystal packing. Specifically, the presence of strong intermolecular hydrogen bonds and a higher incidence of H–π interactions in the aromatic species introduces highly efficient non-radiative decay channels. Conversely, the hydrogenated derivatives lack such interactions, thus preserving their radiative capacity. To describe this specific phenomenon, where fluorescence is increased by the lattice interactions between structurally similar molecules, we have introduced the term packing-induced fluorescence enhancement (PIFE). Given their straightforward synthesis and exceptional optical performance, these hydrogenated derivatives emerge as excellent candidates for optoelectronic applications, particularly as Luminescent Down Shifting (LDS) layers for photovoltaic devices or as emissive layers in blue OLEDs. Furthermore, the identification of the PIFE phenomenon offers a new conceptual framework for the rational design of high-efficiency, solid-state organic luminescent materials.

Author contributions

Chiara Vola: investigation, methodology; G. Attilio Ardizzoia: investigation, software, formal analysis, supervision, funding acquisition, conceptualization, writing – review & editing; Anita Cinco: investigation, methodology; Gioele Colombo: investigation, methodology, data curation, conceptualization, supervision, formal analysis, writing – original draft, writing – review & editing; Bruno Therrien: investigation, formal analysis, writing – review & editing; Stefano Brenna: conceptualization, supervision, writing – review & editing; funding acquisition.

Conflicts of interest

There are no conflicts to declare.

Data availability

The data supporting this article have been included as part of the supplementary information (SI). Supplementary information: Fig. S1: pictures of compounds **2a–e** taken under normal and UV light.; Fig. S2: **2a–e** recorded in solid stateabsorption and emission spectra of compounds **2a–e** recorded in solid state; Fig. S3: linear trend between Hammet's σ para *vs*. emission maxima of compounds **2a–e**; Fig. S4: normalized fluorescence decay curves for compounds **2a–e** recorded in the solid state; Fig. S5: representation of the angles between the planes of the phenol and imidazole moieties in compounds **2a**, **2c** and **1a**; Fig. S6: crystal structure of compounds **1a**, **2a** and **2c** displaying centroid-centroid distances and hydrogen bond distances; Fig. S7: crystal structure of compounds **2a** highlighting the π–π stacking; Fig. S9: Hirshfeld surface analysis for compound **2c** displaying molecular orientation, fingerprint plot, Hirshfeld surface plotted with the d_e color map, Hirshfeld surface plotted with the curvedness color map and Hirshfeld surface plotted with the shape index color map; Table S1: crystallographic and structure refinement parameters for **1a**, **2a** and **2c**. xlsx file: raw data for quantum yield calculation. See DOI: https://doi.org/10.1039/d6cp02388f.

CCDC 2535601 (**1a**), 2535602 (**2a**) and 2535603 (**2c**) contain the supplementary crystallographic data for this paper.[76a–c]

Acknowledgements

The authors thank the Ministero dell'Università e della Ricerca (MUR) and the University of Insubria for funding. Scientific support from CRIETT Center of University of Insubria (instruments code: MAC-01, -04, -06, -12, -13) is greatly acknowledged. This paper and related research have been partly conducted during and with the support of the Italian national inter-university PhD course in Sustainable Development and Climate change (link: https://www.phd-sdc.it) at the University School for Advanced Studies IUSS Pavia, Cycle XXXVIII, with the support of a scholarship financed by the Ministerial Decree no. 351 of 9th April 2022, based on the NRRP – funded by the European Union – NextGenerationEU – Mission 4 ''Education and Research'', Component 1 ''Enhancement of the offer of educational services: from nurseries to universities'' – Investment 4.1 ''Extension of the number of research doctorates and innovative doctorates for public administration and cultural heritage'' (AC).

References

1 R. V. Fernandes, A. Urbano, J. L. Duarte, N. Bristow, J. Ketlle and E. Laureto, *J. Lumin.*, 2018, **203**, 165.
2 A. P. Perdomo, R. V. Fernandes, N. J. Artico Cordeiro, F. Franchello, M. A. Toledo da Silva, J. L. Duarte and E. Laureto, *J. Appl. Phys.*, 2020, **128**, 035502.
3 R. V. Fernandes, N. A. Cordeiro Junior, A. D. Pardo Perdomo, J. L. Duarte and E. Laureto, *Dyes Pigm.*, 2019, **169**, 1.
4 E. Klampaftis, D. Ross, K. R. McIntosh and B. S. Richards, *Sol. Energy Mater. Sol. Cells*, 2009, **93**, 1182.
5 D. Alonso-Álvarez, D. Ross, E. Klampaftis, K. R. McIntosh, S. Jia, P. Storiz, T. Stolz and B. S. Richards, *Prog. Photoboly.: Res. Appl.*, 2014, **23**, 479.
6 N. K. Kalluvettukuzhy, M. R. Maciejczyk, I. Underwood and N. Robertson, *J. Mater. Chem. A*, 2023, **11**, 13195.
7 C. Chen, S. Zheng and H. Song, *Chem. Soc. Rev.*, 2021, **12**, 7250.
8 A. Mayavan, *ACS Omega*, 2024, **9**, 16880.
9 M. Alexandre, M. Chapa, S. Haque, M. J. Mendes, H. Águas, E. Fortunato and R. Martins, *ACS Appl. Energy Mater.*, 2019, **2**, 2930.
10 M. F. Ayala, S. Chandra, B. Cass and S. J. McCormack, Defining Critical Parameters in a Luminescent Downshifting Layer for PV Enhancement, in *Sustainable Energy Development and Innovation. Innovative Renewable Energy*, ed. A. Sayigh, Springer, 2022, pp. 865–870.
11 A. Azaid, M. Raftani, M. Alaqarbeh, R. Kacimi, T. Abram, Y. Khaddam, D. Nebbach, A. Sbai, T. Lakhlifi and M. Bouachrine, *RSC Adv.*, 2022, **12**, 30626.
12 H. Liu, G. Jiang, G. Ke, T.-B. Ren and L. Yuan, *ChemPhotoChem*, 2023, **8**, e202300277.
13 N. N. M. Y. Chan, A. Idris, Z. H. Z. Abidin, H. A. Tajuddin and Z. Abdullah, *RSC Adv.*, 2021, **11**, 13409.
14 S. Kappaun, C. Slugovc and E. J. W. List, *Int. J. Mol. Sci.*, 2008, **9**, 1527.
15 C. W. Tang and S. A. VanSlyke, *Appl. Phys. Lett.*, 1987, **51**, 913.
16 J. Bauri, R. B. Choudhary and G. Mandal, *J. Mater. Sci.*, 2021, **56**, 18837.
17 H. Sasabe and J. Kido, *J. Mater. Chem. C*, 2013, **1**, 1699.
18 E. U. Mughal, N. Naeem, S. F. Kainat, A. M. Almohyawi, J. Qurban, A. Sadiq, A. Abd-El-Aziz, N. Ma, A. S. Abd-El-Aziz, A. Timoumi, Z. Moussa, S. S. A. Natto and S. A. Ahmed, *J. Photochem. Photobiol., C*, 2025, **64**, 100700.
19 C. Yin, Y. Xin, T. Huang, Q. Zhang, L. Duan and D. Zhang, *Nat. Commun.*, 2025, **16**, 30.
20 A. Zhou, H. Wang, Y. Zhang and C. Hu, *Fiber Integr. Opt.*, 2022, **41**, 1.
21 E. H. Cho, Y. W. Kim, J. Sim, H. Yeon, S. Baek, S. M. Jeong, J. Lee, Y. Jeon and K. C. Choi, *Mater. Horiz.*, 2025, **12**, 8862.
22 J. Y. Woo, M.-H. Park, S.-H. Jeong, Y.-H. Kim, B. Kim, T.-W. Lee and T.-H. Han, *Adv. Mater.*, 2022, **35**, 2207454.
23 C. Kant, A. Shukla, S. K. M. McGregor, S.-C. Lo, E. B. Namdas and M. Katiyar, *Nat. Commun.*, 2023, **14**, 7220.
24 H. Dong, B. S. T. Tam, L. Ding and S.-C. Dong, *J. Lumin.*, 2022, **252**, 119360.
25 B. S. T. Tam, S.-C. Dong and C. W. Tang, *J. Semicond.*, 2023, **44**, 092602.
26 Y. Huang, *J. Phys.: Conf. Ser.*, 2023, **2608**, 12012.
27 G. Hong, X. Gan, C. Leonhardt, Z. Zhang, J. Seibert, J. M. Busch and S. Bräse, *Adv. Mater.*, 2021, **33**, 2005630.
28 J. Bauri, R. B. Choudhary and G. Mandal, *J. Mater. Sci.*, 2021, **56**, 18837.
29 B. Geffroy, P. le Roy and C. Prat, *Polym. Int.*, 2006, **55**, 572.
30 R. Singh, P. Singh, B. Sridhar and G. Kaushik, *J. Phys.: Conf. Ser.*, 2024, **2837**, 012031.
31 P. L. dos Santos, P. Stachelek, Y. Takeda and P. Pander, *Mater. Chem. Front.*, 2024, **8**, 1731.
32 R. Liguori, F. Nunziata, S. Aprano and M. G. Maglione, *Electronics*, 2024, **13**, 1299.
33 K. Kumar, *React. Chem. Eng.*, 2024, **9**, 496.
34 I. Siddiqui, S. Kumar, Y.-F. Tsai, P. Gautam, S. K. Kesavan, J.-T. Lin, L. Khai, K.-H. chuo, A. Choudhury, S. Grigalevicius and J.-H. Jou, *Nanomaterials*, 2023, **13**, 2521.
35 Q.-Y. Meng, X.-L. Wen and J. Qiao, *J. Phys. Chem. Lett.*, 2024, **15**, 12571.
36 Y. Im, S. Y. Byung, J. H. Kim, D. R. Lee, C. S. Oh, K. S. Yook and J. Y. Lee, *Adv. Funct. Mater.*, 2017, **27**, 1603007.
37 X. Yang, G. Mu, K. Weng and X. Tang, *Photonics*, 2024, **11**, 864.
38 E. Tankelevičiūtė, I. D. W. Samuel and E. Zysman-Colman, *J. Phys. Chem. Lett.*, 2024, **15**, 1034.
39 J.-H. Lee, C.-H. Chen, P.-H. Lee, H.-Y. Lin, M.-K. Leung, T.-L. Chiu and C.-F. Lin, *J. Mater. Chem. C*, 2019, **7**, 5874.
40 R. Gopathi, M. P. Kumar, G. J. Kumar, N. P. Srymprasad, B. G. Kodiripaka, V. G. M. Naidu and B. N. Babu, *RSC Med. Chem.*, 2025, **16**, 1188.
41 K. B. Alapati, D. Sravani, S. Gouthamsri, B. B. V. Sailaja, B. Saritha and S. Nalla, *Chem. Data Coll.*, 2024, **54**, 101162.
42 M. R. Reddy, C. M. Darapaneni, R. D. Patil and H. Kumari, *Org. Biomol. Chem.*, 2022, **20**, 3440.
43 G. Volpi, *Asian J. Org. Chem.*, 2022, **11**, e202200171.

44 G. Colombo, G. A. Ardizzoia and S. Brenna, *Inorg. Chim. Acta*, 2022, **535**, 120849.
45 X. Kong, J. Zhao, L. Yang, F. Wang and Z. Sun, *Anal. Bioanal. Chem.*, 2024, **416**, 329.
46 R. Cui, C. Liu, P. Zhang, K. Qin and Y. Ge, *Molecules*, 2023, **28**, 515.
47 A. Cinco, C. Vola, G. A. Ardizzoia, S. Brenna and G. Colombo, *Appl. Sci.*, 2026, **16**, 1937.
48 G. Colombo, G. A. Ardizzoia, J. Furrer, B. Therrien and S. Brenna, *Chem. – Eur. J.*, 2021, **27**, 12380.
49 G. Colombo, A. Cinco, G. A. Ardizzoia and S. Brenna, *Colorants*, 2023, **2**, 179.
50 G. Colombo, A. Cinco, S. Brenna, J. Furrer, B. Therrien and G. A. Ardizzoia, *Dyes Pigm.*, 2023, **220**, 111722.
51 G. Colombo, A. Cinco, C. Vola, B. Therrien, G. A. Ardizzoia and S. Brenna, *Eur. J. Inorg. Chem.*, 2024, e202400251.
52 A. Cinco, G. A. Ardizzoia, S. Brenna, B. Therrien and G. Colombo, *Molecules*, 2025, **30**, 2552.
53 A. Cinco, G. Colombo, S. Brenna, C. Vola, B. Therrien and G. A. Ardizzoia, *Precis. Chem.*, 2026, DOI: 10.1021/prechem.6c00034.
54 A. Marchesi, S. Brenna and G. A. Ardizzoia, *Dyes Pigm.*, 2019, **161**, 457.
55 G. Colombo, A. Romeo, G. A. Ardizzoia, J. Furrer, B. Therrien and S. Brenna, *Dyes Pigm.*, 2020, **182**, 108636.
56 M. Stanitska, N. Pokhodylo, R. Lytvyn, E. Urbonas, D. Volyniuk, S. Kutsiy, K. Ivaniuk, V. Kinzhybalo, P. Stakhira, R. Keruckiene, M. Obushak and J. A. Gražulevičius, *ACS Omega*, 2024, **9**, 14613.
57 K. Maleckaitė, D. Narkevičius, R. Žilėnaitė, J. Dodonova-Vaitkūnienė, S. Toliautas, S. Tumkevičius and A. Vyšniauskas, *Molecules*, 2022, **27**, 23.
58 H. Tezcan and S. Ozkan, *Dyes Pigm.*, 2003, **56**, 159.
59 K. Kemnitz, N. Tamai, I. Yamazaki, N. Nakashima and K. Yoshihara, *J. Phys. Chem.*, 1987, **91**, 1423.
60 L. Wang, Y. Huang, A. Waleed, K. Wu, C. Lin, Z. Wang, G. Zheng, Z. Fan, J. Sun, H. Zhou, L.-D. Sun and C.-H. Yan, *ACS Appl. Mater. Interfaces*, 2017, **9**, 25985.
61 J. Wu, M. He, C. Liu and P. Gao, *Adv. Photon. Res.*, 2024, **6**, 2400110.
62 Y. Yamaguchi, Y. Matsubara, T. Ochi, T. Wakamiya and Z.-I. Yoshida, *J. Am. Chem. Soc.*, 2008, **130**, 138867.
63 V. L. Emolaev, *Opt. Spectrosc.*, 2016, **121**, 567.
64 J. P. Dinnocenzo, O. Haze, C. Fleming and S. Farid, *J. Phys. Chem. A*, 2024, **128**, 10986.
65 M. A. Spackman and D. Jayatilaka, *CrystEngComm*, 2009, **11**, 19.
66 K. Shirai, M. Marsuoka and K. Fukunishi, *Dyes Pigm.*, 1999, **42**, 95.
67 Y. Shao, G.-Z. Yin, X. Ren, X. Zhang, J. Wang, K. Guo, X. Li, C. Wesdemiotis, W.-B. Zhang, S. Yang, M. Zhu and B. Sun, *RSC Adv.*, 2017, **7**, 6530.
68 I. Knysh, A. Kozakiewicz-Piekarz, A. Wojtczak, D. Plażuk, G. Baryshnikov, R. Valiev, R. Nasibullin, H. Ågren, D. Jacquemin, B. Ośmiałowski and R. Zaleśny, *J. Mater. Chem. C*, 2021, **9**, 15820.
69 G.-J. Zhao and K.-L. Han, *Acc. Chem. Res.*, 2012, **45**, 404.
70 Y. Li, C. Sun, J. Han, Q. Zhou, B. Cao, H. Yin and Y. Shi, *J. Lumin.*, 2020, **221**, 117110.
71 T. Hossen and K. Sahu, *J. Phys. Chem. A*, 2018, **122**, 2394.
72 L.-O. Pålsson and A. Monkman, *Adv. Mater.*, 2002, **14**, 757.
73 O. V. Dolomanov, L. J. Bourhis, R. J. Gildea, J. A. K. Howard and A. Puschmann, *J. Appl. Crystallogr.*, 2009, **42**, 339.
74 C. F. Macrae, I. Sovago, S. J. Cottrell, P. T. A. Galek, P. McCabe, E. Pidcock, M. Platings, G. P. Shields, J. S. Stevens, M. Towler and P. A. Wood, *J. Appl. Crystallogr.*, 2020, **53**, 226.
75 S. K. Wolff, D. J. Grimwood, J. J. McKinnon, M. J. Turner, D. Jayatilaka and M. A. Spackman, *Crystal explorer*, 2012.
76 (*a*) CCDC 2535601: Experimental Crystal Structure Determination, 2026, DOI: 10.5517/ccdc.csd.cc2r3hlz; (*b*) CCDC 2535602: Experimental Crystal Structure Determination, 2026, DOI: 10.5517/ccdc.csd.cc2r3hm0; (*c*) CCDC 2535603: Experimental Crystal Structure Determination, 2026, DOI: 10.5517/ccdc.csd.cc2r3hn1.